Journal of Solid State Chemistry **164,** 71–80 (2002)
doi:10.1006/jssc.2001.9449, available online at http://www.idealibrary.com on IDEAL®

Crystal Structure and Magnetic Properties of a New Iron(III) Silicophosphate $Fe_3P_5SiO_{19}$ Studied by Neutron Diffraction and Mössbauer Techniques

L. K. Elbouaanani,* B. Malaman,* R. Gérardin,*,[1] and B. Ouladdiaf†

*Laboratoire de Chimie du Solide Minéral, Université Henri Poincaré-Nancy 1, associé au CNRS (UMR 7555), B.P. 239, 54506 Vandoeuvre-les-Nancy Cedex, France; and †Institut Laue-Langevin, B.P. 156, 38042 Grenoble Cedex 9, France

Received July 10, 2001; in revised form October 25, 2001; accepted November 9, 2001

$Fe_3P_5SiO_{19}$ has been prepared by solid state reaction of $Fe(PO_3)_3$, $FePO_4$, and SiO_2 at 1000°C. The structure has been determined from a single crystal through direct methods and difference Fourier synthesis and refined to $R = 0.052$. The unit cell is hexagonal, space group $P6_3$, with $a = 14.4804(8)$ Å, $c = 7.4256(2)$ Å, and $Z = 4$. The three-dimensional framework is built up from $[Fe_2O_9]$ units of two faces sharing octahedra and Si_2O_7 disilicates linked by PO_4 tetrahedra. $Fe_3P_5SiO_{19}$ is isotypic with $V_3P_5SiO_{19}$. $Fe_3P_5SiO_{19}$ is antiferromagnetic below $T_N = 35$ K. The magnetic structure has been determined by means of powder neutron diffraction methods: the magnetic moments are antiferromagnetically coupled inside the $[Fe_2O_9]$ units, in agreement with the Goodenough rules. These units are linked to each other through several Fe–O–P–O–Fe super-superexchange pathways and form antiferromagnetic [001] rows. The moment direction lies in the (001) plane ($\mu_{Fe} = 4.56(5)$ μ_B at 2 K). There is a competition between the intra- and interunits interactions which all are antiferromagnetic and cannot be simultaneously satisfied without frustration. Mössbauer spectra are fitted with two doublets and two sextuplets in the paramagnetic and antiferromagnetic states, respectively. Their rather high isomer shifts are explained by the inductive effect. The magnetic interactions are discussed.

Key Words: **iron silicophosphate; crystal structure; neutron diffraction; magnetic structure; ^{57}Fe Mössbauer spectrometry.**

INTRODUCTION

In the Fe–P–Si–O system, only two phases have been known until now: iron(III) FeP_3SiO_{11} studied by Elbouaanani *et al.* (1) and iron(II) $Fe_2SiP_4O_{14}$ described by Glaum and Schmidt (2).

In the course of an investigation of mixed-valent iron phosphates and silicophosphates, we have discovered a new iron(III) silicophosphate: $Fe_3P_5SiO_{19}$. This work shows that it is isotypic with $V_3P_5SiO_{19}$ whose the crystallographic structure was established by Leclaire *et al.* (3). There also exists $Mo_3P_5SiO_{19}$ synthesized by Wang *et al.* (4) but the crystallographic structure of $Mo_3P_5SiO_{19}$ differs from that of $V_3P_5SiO_{19}$ in the position of one P atom. These two compounds crystallize in the space group $P6_3$ with $Z = 4$. V(III) and Mo(III) are in confacial bioctahedral units $[V_2O_9]$ and $[Mo_2O_9]$ where V–V and Mo–Mo distances are rather short; for the latter Wang *et al.* (4) expect a Mo–Mo bond.

In this Paper, we present the crystallographic and magnetic structures of $Fe_3P_5SiO_{19}$ determined by means of single-crystal X-ray diffraction, bulk magnetization, powder neutron diffraction, and Mössbauer spectroscopy experiments. It will be interesting to compare the magnetic structure of $Fe_3P_5SiO_{19}$ to those of $V_3P_5SiO_{19}$ and $Mo_3P_5SiO_{19}$, which are not yet known today.

EXPERIMENTAL

$Fe_3P_5SiO_{19}$ has been obtained from the "$Fe(PO_3)_3$/$FePO_4$/SiO_2" mixture in adequate proportions, annealed for 3 days at 1000°C, in a silica tube. The starting compounds were prepared as follows.

$Fe(PO_3)_3$ and $FePO_4$ were obtained from a solution of $Fe(NO_3)_3 \cdot 9H_2O$ and H_3PO_4 (in the ratio $Fe/P = \frac{1}{3}$ and $Fe/P = \frac{1}{1}$, respectively), which was evaporated, and then annealed at 400°C under nitrogen for 24 h and finally annealed at 900°C under oxygen.

SiO_2 was obtained from silicic acid $SiO_2 \cdot xH_2O$ annealed at 120°C to eliminate water and then annealed at 800°C for 12 h.

Single crystals were grown by long annealing (1 month) in sealed silica tubes within a gold crucible, under vacuum, at 1000°C, with traces of $FeCl_2$ as mineralizing agent. A single crystal ($\phi \sim 100$ μm) was selected for the structure

[1]To whom correspondence should be addressed. E-mail: Rene.Gerardin@lcsm.uhp-nancy.fr.

0022-4596/02 $35.00

determination. The data were collected on a Nonius Kappa-CCD area detector diffractometer at the Service Commun de Diffractométrie de l'Université Henri Poincaré-Nancy I.

Magnetic measurements were performed (between 4.2 and 300 K) on a MANICS magnetosusceptometer in fields up to 1.6 T.

Neutron diffraction experiments were carried out at the Institut Laue Langevin, Grenoble. Several diffraction patterns were recorded with the one-dimensional curved multidetector D1B using a neutron wavelength of 2.520 Å, in the temperature range 100–2 K. The analysis of the patterns was performed by Rietveld profile refinements (5) using the software Fullprof (6).

The Mössbauer data were collected with a constant acceleration spectrometer with 1024 channels. Isomer shifts are reported with respect to α-iron at room temperature (line width = 0.25 mm/s). The Mössbauer effect data were analyzed by using least-squares minimization techniques (7) to evaluate the hyperfine spectral parameters.

STRUCTURE DETERMINATION

The cell parameters, initially measured on Guinier pattern, were refined by diffractometric techniques at 20°C with least-squares refinement based on 25 reflections and are $a = 14.4804(8)$ Å, $c = 7.4256(2)$ Å in the hexagonal system.

From the data collection containing 5840 reflections, 895 with $I > 3\sigma(I)$ were considered for the structural resolution.

TABLE 1
Summary of Data Collection and Structure Refinement of $Fe_3P_5SiO_{19}$

Molar mass (g.mol^{-1})	654.49
Crystal size (μm)	$\varphi \approx 100$
Symmetry	Hexagonal
a (Å)	14.4804(8)
c (Å)	7.4256(2)
V (Å^3)	1347.39
Z	4
ρ_{cal} (g.cm^{-3})	3.251
Space group	$P6_3$
Radiation	Mo$K\alpha$
Monochromator	Graphite
Scan mode	Oscillation scan
Record limits (°)	$\theta \leq 25$
Linear absorption coefficient μ (mm^{-1})	133.67
Recorded intensities	5840
Unique and nonzero intensities	2078
Recorded intensities with $\sigma(I)/I < 0.33$	895
$F(000)$	1276
Index ranges	$0 \leq h \leq 14$. $0 \leq k \leq 14$. $-7 \leq l \leq 7$
Number of parameters	79
Final R value	0.052
Final w$R2$ value	0.052

TABLE 2
Atomic Coordinates and Thermal Agitation Factors for $Fe_3P_5SiO_{19}$

Atom	Site	Symmetry	x	y	z	B(Å^2)
Fe(1)	6c	1	0.3409(5)	0.0173(5)	0.1892[a]	0.79(8)
Fe(2)	6c	1	0.3411(4)	0.0182(5)	0.7826(4)	0.79(8)
P(1)	6c	1	0.1466(3)	−0.0868(3)	0.4864(17)	0.58(6)
P(2)	6c	1	0.4329(3)	0.2120(3)	0.4875(17)	0.66(6)
P(3)	6c	1	0.4228(3)	−0.0957(3)	0.4852(18)	0.59(6)
P(4)	2a	3	0	0	0.4503(18)	1.18(16)
Si(1)	2b	3	$\frac{2}{3}$	$\frac{1}{3}$	0.5274(19)	1.26(24)
Si(2)	2b	3	$\frac{1}{3}$	$\frac{2}{3}$	0.4590(17)	0.95(16)
O(1)	6c	1	0.2516(13)	0.2110(13)	0.1551(24)	0.01(3)
O(2)	6c	1	0.3634(8)	0.2657(7)	0.4851(38)	0.55(16)
O(3)	6c	1	0.4512(16)	0.3969(16)	0.1552(30)	1.03(39)
O(4)	6c	1	0.6955(8)	0.9042(7)	0.4841(43)	0.47(16)
O(5)	6c	1	0.0600(8)	0.6021(8)	0.4953(31)	0.47(24)
O(6)	6c	1	0.2005(18)	0.9660(18)	0.3108(32)	1.97(47)
O(7)	6c	1	0.6918(9)	0.2440(9)	0.4746(36)	1.50(24)
O(8)	6c	1	0.4228(16)	0.1515(16)	0.3270(29)	1.10(39)
O(9)	6c	1	0.0719(17)	0.4573(17)	0.3113(30)	1.66(47)
O(10)	6c	1	0.2655(17)	0.4148(17)	0.1686(33)	1.10(39)
O(11)	6c	1	0.1181(9)	0.0493(9)	0.0213(23)	1.03(24)
O(12)	6c	1	0.6402(10)	0.2198(10)	0.0264(21)	1.26(31)
O(13)	2a	3	0	0	0.240(15)	1.7(9)
O(14)	2b	3	$\frac{2}{3}$	$\frac{1}{3}$	0.7411(40)	1.26(47)

[a]Atom used to fix the origin of the cell

The choice of space group according to the conditions limiting possible reflections (00l with $l = 2n$) was between $P6_3$, $P6_3/m$, and $P6_322$.

The conditions for the data collection and refinement of the structure are listed in Table 1. All computer programs used were taken from Ref. (8). Absorption was corrected by the Sortav software (9). Scattering factors for Fe, P, Si, and O were taken from the *International Tables for X-ray Crystallography* (10).

The structure was refined satisfactorily in the space group $P6_3$. The iron, phosphorus, and silicon atom positions have been obtained using the direct methods procedure of the Shelx program (8). The oxygen atom positions were determined by difference Fourier synthesis. Final refinement with individual and isotropic temperature factors leads to the reliability factors $R = 0.052$ ($R_w = 0.052$). The atomic parameters are listed in Table 2 and the main interatomic distances and angles are given in Table 3.

STRUCTURE DESCRIPTION

The crystal structure of $Fe_3P_5SiO_{19}$ is a three-dimensional network of corner-sharing [Fe_2O_9] units, PO_4 tetrahedra, and disilicate Si_2O_7 groups (Fig. 1). The [Fe_2O_9] unit is formed by pair of FeO_6 octahedra sharing a face; the Si_2O_7 disilicate group is formed by a pair of SiO_4 tetrahedra sharing an apex and exhibiting a semieclipsed

TABLE 3
Main Interatomic Distances (Å) and Angles (°) for $Fe_3P_5SiO_{19}$

	[FeO_6] octahedra		
Fe(1)–O(9)	1.93(2)	Fe(2)–O(10)	1.85(3)
Fe(1)–O(8)	1.98(2)	Fe(2)–O(3)	1.87(2)
Fe(1)–O(6)	2.00(2)	Fe(2)–O(1)	1.89(2)
Fe(1)–O(5)	2.06(2)	Fe(2)–O(4)	2.09(2)
Fe(1)–O(2)	2.11(2)	Fe(2)–O(2)	2.11(2)
Fe(1)–O(4)	2.12(2)	Fe(2)–O(5)	2.17(2)
$\overline{Fe(1)–O}$	2.03	$\overline{Fe(2)–O}$	2.00
	Fe(1)–Fe(2) 3.019(3)		
	[PO_4] Tetrahedra		
P(1)–O(1)	1.50(2)	P(2)–O(8)	1.44(2)
P(1)–O(6)	1.52(2)	P(2)–O(2)	1.55(1)
P(1)–O(4)	1.54(1)	P(2)–O(10)	1.57(3)
P(1)–O(11)	1.58(1)	P(2)–O(7)	1.59(2)
$\overline{P(1)–O}$	1.54	$\overline{P(2)–O}$	1.54
P(3)–O(9)	1.51(2)	P(4)–O(13)	1.56(11)
P(3)–O(3)	1.52(2)	P(4)–O(11) × 3	1.58(1)
P(3)–O(5)	1.54(1)		
P(3)–O(12)	1.59(1)		
$\overline{P(3)–O}$	1.54	$\overline{P(4)–O}$	1.56
	[SiO_4] Tetrahedra		
Si(1)–O(7) × 3	1.56(2)	Si(2)–O(12) × 3	1.57(2)
Si(1)–O(14)	1.59(3)	Si(2)–O(14)	1.62(3)
$\overline{Si(1)–O}$	1.58	$\overline{Si(2)–O}$	1.58
	Angles		
Si(1)–O(7)–P(2)	139(1)	Si(2)–O(12)–P(3)	146(1)
P(4)–O(11)–P(1)	141(1)	Si(1)–O(14)–Si(2)	180

configuration. The six terminal oxygen atoms of Si_2O_7 are bonded to six surrounding PO_4 tetrahedra: three P(2)O_4 and three P(3)O_4, forming the [$Si_2P_6O_{25}$] silicophosphate unit.

The [Fe_2O_9] units and the Si_2O_7 disilicates are along infinite rows parallel to the *c* axis, connected to each other by PO_4 tetrahedra (Fig. 2).

The two FeO_6 octaedra are distorted. They exhibit three short distances Fe–O, 1.85 to 2.00 Å, values smaller than the 2.015 Å calculated by Brown and Altermatt (11) for the bond length Fe^{3+}_{oct}–O^{2-}. Three longer distances, 2.06 to 2.17 Å, connect each Fe atom to the three O atoms O(2), O(4), and O(5) of the shared face (see Table 3).

The distance Fe–Fe (3.019 Å) is comparable to 2.967 and 3.048 Å, values found in $Fe_4(P_2O_7)_3$ by Elbouaanani *et al.* (12), and 2.99 Å found in the $Fe_4(PO_4)_3(OH)_3$ hydroxyphosphate compound by Ijjaali *et al.* (13).

Face-sharing between octahedra is much less common in iron compounds than edge-sharing, because it brings cations very close to each other and this destabilizes the lattice. But for this compound, as we are dealing with distorted octahedra, the Fe^{3+} ions move in such a way that they increase their distance from each other to 3.019 Å, which is comparable to what we have in edge-sharing octahedra.

Simultaneously, oxygen ions move within the shared face toward each other in order to screen the Fe^{3+}–Fe^{3+} repulsion. The mean oxygen–oxygen distance is significantly smaller in the shared face, $\overline{O–O} = 2.55$ Å between O(2)–O(4)–O(5), whereas $\overline{O–O} = 2.99$ Å between O(9)–O(8)–O(6) face and 2.83 Å for the O(1)–O(3)–O(10) face (see Fig. 2).

The P(4) atom (special position (2*a*), Table 2) is in tetrahedra obviously aligned along the *c* axis. Each P(4)O_4 tetrahedron connects its three apices O(11) with three P(1)O_4 tetrahedra, and the fourth apex O(13) is "free" (O(13) is only bound to P(4)) (Figs. 3 and 4a); in this way these four tetrahedra form the [P_4O_{13}] unit. This situation

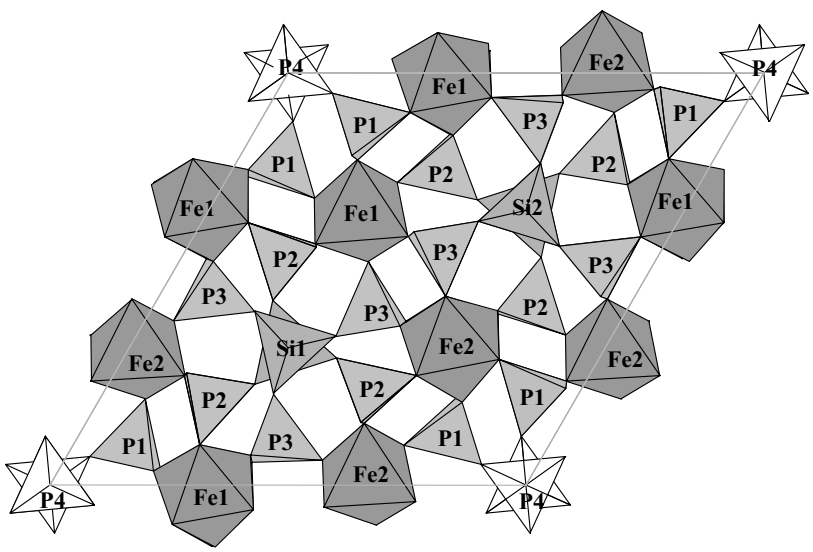

FIG. 1. Projection of the framework of $Fe_3P_5SiO_{19}$ along [001].

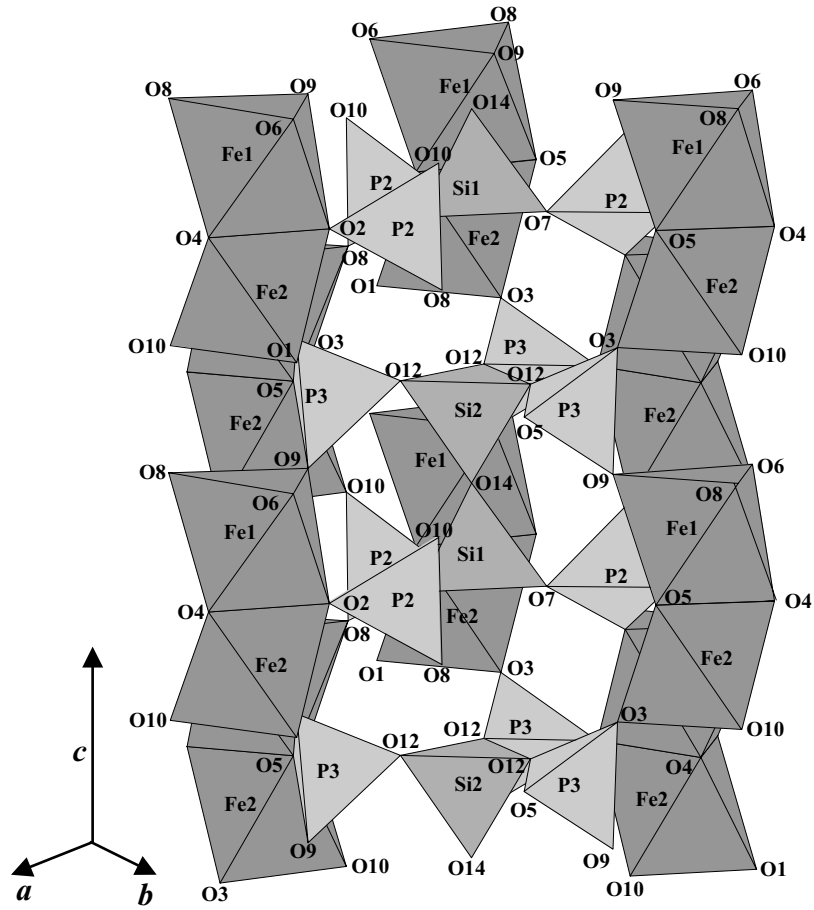

FIG. 2. Clinographic view showing the connections between Si_2O_7 and $[Fe_2O_9]$ units via $P(2)O_4$ and $P(3)O_4$ tetrahedra.

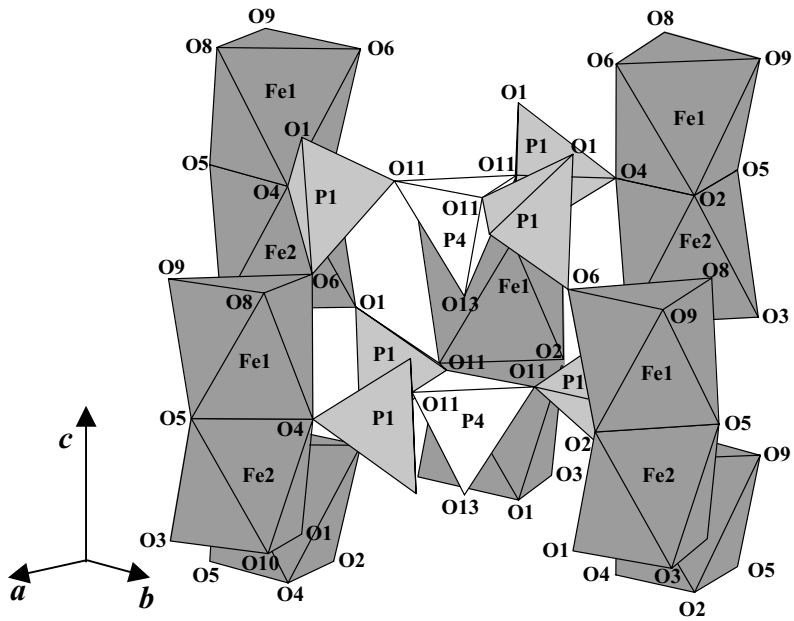

FIG. 3. Clinographic view showing the connections between $P(4)O_4$ and $[Fe_2O_9]$ units via $P(1)O_4$ tetrahedra.

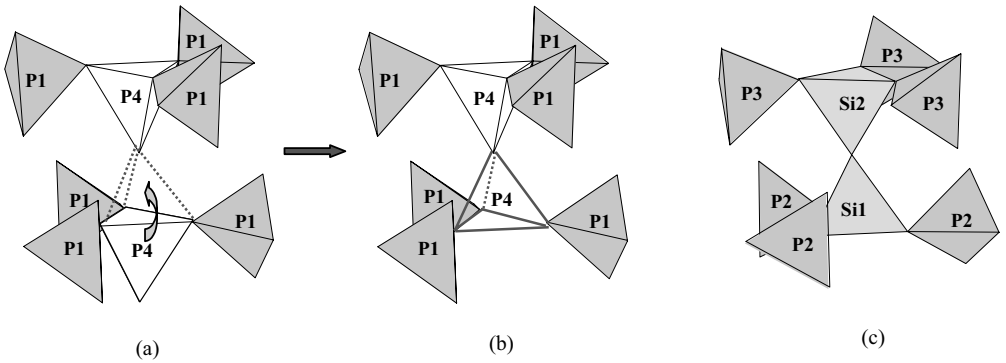

FIG. 4. (a) Real $[P_4O_{13}]$ unit. (b) Hypothetical $[P_8O_{25}]$ unit. (c) Real $[Si_2P_6O_{25}]$ unit.

is not usual, it is also found in $V_3P_5SiO_{19}$ (3). The three distances P(4)–O(11) = 1.58(1) Å seem to be longer than P(4)–O(13) = 1.56(11) Å (it is the opposite in $V_3P_5SiO_{19}$: respectively three 1.517(5) and one 1.54(4) Å). In the two cases the low accuracy on the distance values $P–O_{free}$ can be explained by a high thermal agitation. This phenomenon also exists in $Mo_3P_5SiO_{19}$ but was interpreted differently by Wang *et al.* (4): two sites P(4) and P′(4), 0.55 Å apart, with the occupancy factors 0.55 and 0.45 are used to place this P atom in the cell. Whatever way we look at the problem, these structural determinations should reflect a structural disorder on this point.

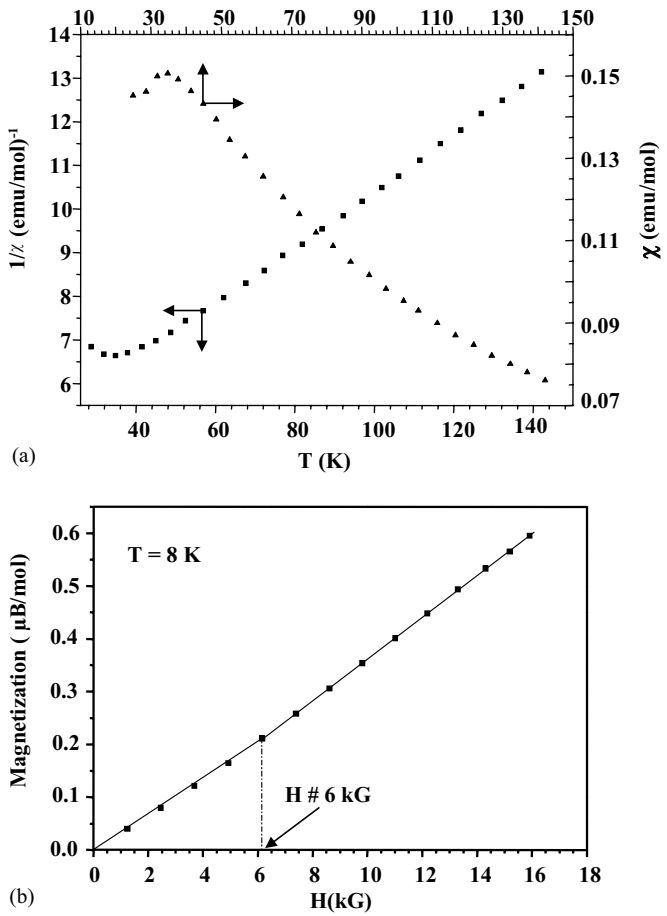

FIG. 5. (a) Temperature dependence of the inverse susceptibility of $Fe_3P_5SiO_{19}$, (b) Magnetization versus applied field of $Fe_3P_5SiO_{19}$ at 8 K.

Two adjacent $P(4)O_4$ groups are eclipsed (see Fig. 1) and, like in $[Si_2P_6O_{25}]$, $[P_4O_{13}]$ connects $[Fe_2O_9]$ units (Fig. 3).

The P–O distances for P(1), P(2), and P(3) are classical (Table 3), and the average values (1.54 Å) are comparable to the 1.536 Å value given by Corbridge (14). The longest P–O distances are observed for O common to the PO_4 and SiO_4 tetrahedra, and the same is found for the other silicophosphates (15–17).

The angles Si–O–P involving an oxygen atom bridging two tetrahedra range from 143(1) to 156(2)°, close to the values found in $V_3P_5SiO_{19}$ (3) (134.9(2) and 151.1(4)°).

The staking of the $[P_4O_{13}]$ units along the *c* axis shows that the simple migration of one central phosphorus atom along the P(4)–P(4)--- row (Fig. 4a) would lead to the $[P_8O_{25}]$ units (Fig. 4b). This hypothetical unit does not exist in iron phosphates. The replacement of the two central phosphorus atoms by silicon in the $[P_8O_{25}]$ allows the formation of a $[P_6Si_2O_{25}]$ unit (Fig. 4c). A framework built up from of $[M_2O_9]$ dimers and only $[P_6Si_2O_{25}]$ units exists with the $M_4P_6Si_2O_{25}$ composition for M = Mo (17), but not for M = Fe.

These results show that $Fe_3P_5SiO_{19}$ is isotypic with $V_3P_5SiO_{19}$ (3).

MAGNETIC STUDY

(a) Susceptibility Measurements

The thermal variation of the susceptibility is shown in Fig. 5a. $Fe_3P_5SiO_{19}$ is antiferromagnetic below $T_N = 35$ K. In the paramagnetic state, the Curie–Weiss law is obeyed, leading to the Curie molar constant $C_M = 15.66$, which corresponds to 6.46 μ_B for the effective magnetic moment

per iron atom. This value is higher than 5.9 μ_B expected for a high-spin iron(III) cation. We have no explanation to interpret this difference; however, we have noted that this fact is currently observed for iron(III) phosphate compounds, as the results below show:

$Fe_3(PO_4)_3F_2$, $(CH_3NH_3)_2$, H_2O	6.2(3) μ_B
$Fe(OH)(H_2O)(O_3P–(CH_2)_2–CO_2H)$	6.3(2) μ_B
$C–Fe(PO_3)_3$	6.1 μ_B
$Fe_4(P_2O_7)_3$	6.14 μ_B
FeP_3SiO_{11}	6.08 μ_B

The extrapolated Curie temperature is negative: $\theta_p = -63$ K.

The measurement of the magnetization versus field at 8 K is shown in Fig. 5b. The magnetization increases linearly at low field, and then it changes slope at about $H = 6$ kG. Such behavior may be characteristic of a metamagnetic-like transition.

(b) Neutron Diffraction Study

The patterns recorded and the calculated diffraction profiles at 105 and 2 K are shown in Figs. 6a and 6b.

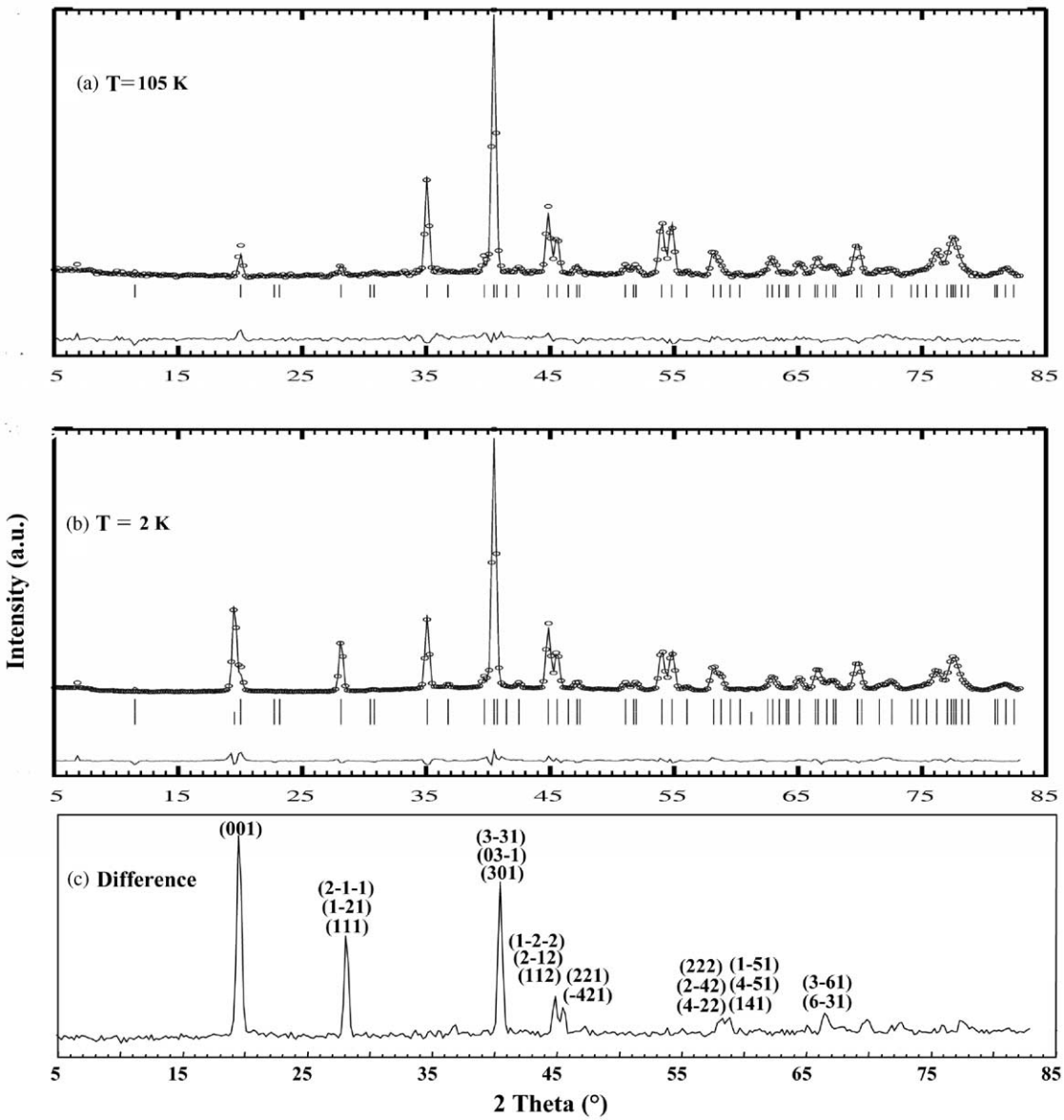

FIG. 6. Observed and calculated neutron powder diffraction profile of $Fe_3P_5SiO_{19}$: (a) at $T = 105$ K, (b) at $T = 2$ K, and (c) difference between the observed spectra collected at 105 and 2 K.

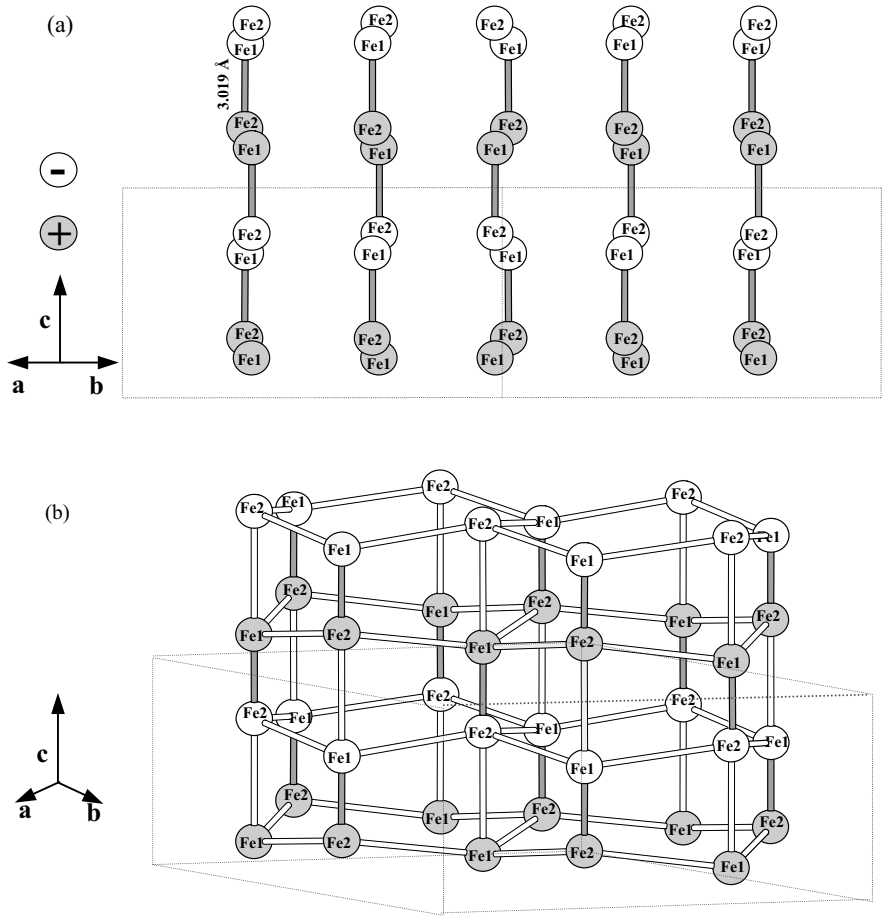

FIG. 7. Collinear arrangement of spin for antiferromagnetic ordering of $Fe_3P_5SiO_{19}$. The gray and white circles indicate opposing spin direction in the *ab* plane. The gray bonds represent the 3.019 Å intradimer $[Fe_2O_9]$ distance. The white bonds represent the 4.41, 4.85, 4.87, and 4.93 Å interdimer $[Fe_2O_9]$ distances. (a) Projection along [110]. (b) Clinographic view.

At 2 K, additional lines, characteristic of an antiferromagnetic ordering, appear in agreement with the magnetic measurements. All of the observed reflections can be indexed in the same crystal unit cell and it was quickly established that additional peaks 00*l* only occur with $l = 2n + 1$ (forbidden by the 6_3 axis (Fig. 6)). The (001) line appears essentially as the strongest one; this implies that the easy magnetization axis probably lies in this plane or in its close neighborhood.

As shown in the previous section, there are two independent iron sites (Table 2) which give two magnetic sublattices, and for each there are six crystallographically equivalent positions per unit cell. The loss of the 6_3 axis leads to an antiferromagnetic arrangement in each Fe sublattice.

All these structural and magnetic considerations suggest an antiferromagnetic structure based on an antiferromagnetic arrangement in each $[Fe_2O_9]$ unit, with the spin direction perpendicular to the [001] direction. The magnetic structure is illustrated in Figs. 7a and 7b.

It should be noted that a full refinement is not possible due to the lack of experimental information, as there are 61 variable parameters to determine from 60 independent neutron data. Therefore, using the set of nuclear parameters defined during the single-crystal X-ray study (Table 2) only, the scale factor, the lattice and half-width parameters, and the magnetic moment components (constrained to be equal for the two independent iron sites) were refined. The best fit to the data is characterized by the standard quantities, $R_{NUC} = 7.9\%$ and $R_{MAG} = 5.6\%$, and gives the value of Fe magnetic moment equal to 4.56(5) μ_B. This value is expected for a high-spin iron(III). The final refinement and the difference spectra between 105 and 2 K are shown in Figs. 6b and 6c.

(c) Mössbauer Study

Paramagnetic state ($T > 35\,K$). The observed spectrum at 295 K is shown in Fig. 8a. The width of each peak is 0.35 mm/s. This value is too great to represent the resonance

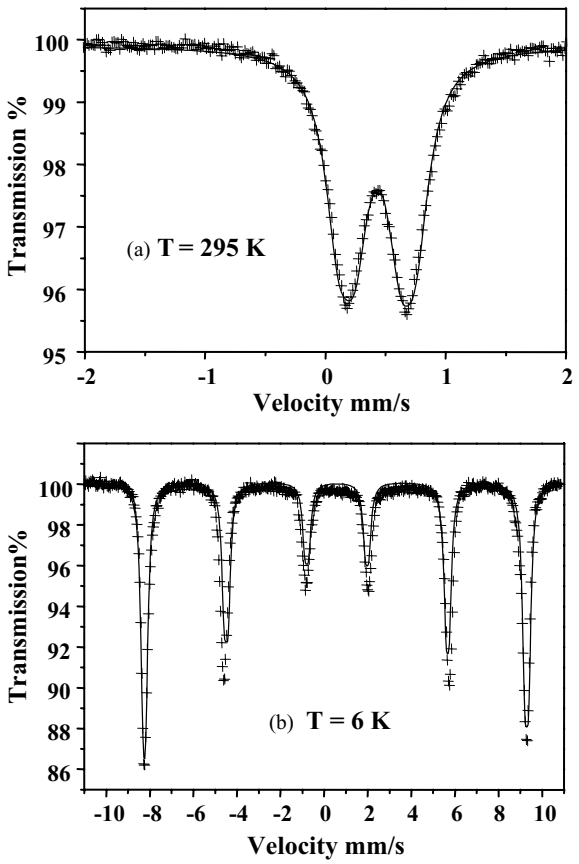

FIG. 8. Mössbauer spectra of $Fe_3P_5SiO_{19}$ at (a) $T = 295$ K and $T = 6$ K.

of one type of iron but is consistent with the resonance of two types. The spectrum was then accurately fitted with two Lorentz-type quadrupole doublets where the intensity of each doublet was constrained to be equal and the widths of the peaks were fixed to 0.27 mm/s. Each doublet is associated with each of the two crystallographically distinct iron sites.

The calculated spectral parameters are presented in Table 4.

The isomer shift values ($\delta = 0.431$ and 0.435 mm/s) are clearly characteristic of the paramagnetic high-spin iron(III) (21). These high values are not unexpected: they are similar to those found in $Fe_4(P_2O_7)_3$ (0.41 to 0.42 mm/s) (12) and it has been well established (22) that, thanks to the inductive

TABLE 4
Mössbauer Spectral Parameters for $Fe_3P_5SiO_{19}$ at 110 K

Site	δ^a (mm.s^{-1})	Δ (mm.s^{-1})	Γ (mm.s^{-1})	I (%)
1	0.431	0.643	0.27	50
2	0.435	0.377	0.27	50

[a]Relative to room temperature α-iron foil $\delta \pm 0.005$, $\Delta \pm 0.005$.

TABLE 5
Mössbauer Spectral Parameters for $Fe_3P_5SiO_{19}$ at 6 K

Site	δ^a (mm.s^{-1})	2ε (mm.s^{-1})	H (T)	Γ (mm.s^{-1})	I (%)
1	0.540	0.096	54.7	0.27	50
2	0.558	−0.216	54.6	0.27	50

[a]Relative to room temperature α-iron foil. $\delta \pm 0.005$, $2\varepsilon \pm 0.005$, $H \pm 0.1$.

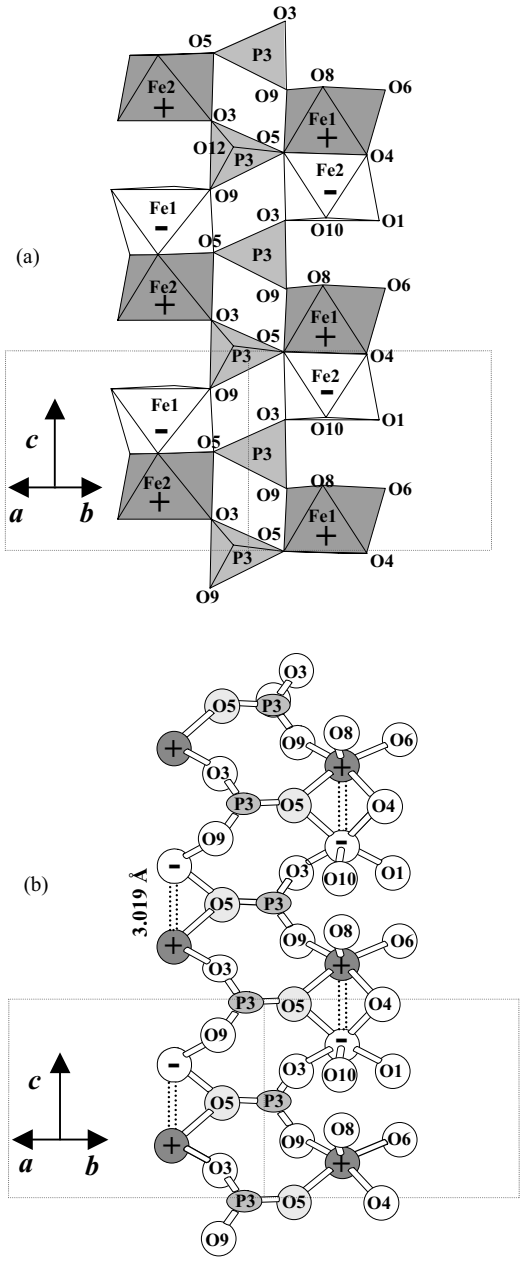

FIG. 9. Projection of the structure of $Fe_3P_5SiO_{19}$ along [110] showing (a) the $[Fe_2O_9]$, PO_4 connections and (b) exchange, superexchange, and super-superexchange paths in $Fe_3P_5SiO_{19}$: intradimer $[Fe_2O_9]$, Fe–Fe and Fe–O–Fe; interdimer $[Fe_2O_9]$ via the $P(3)O_4$ tetrahedra, Fe–O–P–O–Fe.

TABLE 6
Magnetic Interactions in $Fe_3P_5SiO_{19}$

Interaction	Nature	Sign	*n*	Pathway (Å, °)	Fe–Fe Distance (Å)
$Fe^{3+}(1)$–$Fe^{3+}(2)$	Direct	AF	1		3.019
$Fe^{3+}(1)$–O(5)–$Fe^{3+}(2)$	Superexchange	AF	1	4.23, 91	3.019
$Fe^{3+}(1)$–O(2)– $Fe^{3+}(2)$		AF	1	4.22, 92	3.019
$Fe^{3+}(1)$–O(4)–$Fe^{3+}(2)$		AF	1	4.21, 92	3.019
$Fe^{3+}(1)$–O(6)–P(1)–O(1)–$Fe^{3+}(2)$	Super-superexchange	AF	2	6.91, 116	4.41
$Fe^{3+}(2)$–O(1)–P(1)–O(4)–$Fe^{3+}(1)$		F	2	7.05, 111	4.87
$Fe^{3+}(2)$–O(1)–P(1)–O(4)–$Fe^{3+}(2)$		AF	2	7.02, 111	6.08
$Fe^{3+}(1)$–O(6)–P(1)–O(4)–$Fe^{3+}(2)$		F	2	7.15, 114	4.85
$Fe^{3+}(1)$–O(6)–P(1)–O(4)–$Fe^{3+}(1)$		AF	2	7.18, 114	6.08
$Fe^{3+}(1)$–O(8)–P(2)–O(10)– $Fe^{3+}(2)$		AF	2	6.84, 115	4.41
$Fe^{3+}(1)$–O(8)–P(2)–O(2)–$Fe^{3+}(2)$		F	2	7.08, 114	4.87
$Fe^{3+}(1)$–O(8)–P(2)–O(2)–$Fe^{3+}(1)$		AF	2	7.08, 114	6.08
$Fe^{3+}(2)$–O(10)–P(2)–O(2)–$Fe^{3+}(1)$		F	2	7.08, 110	4.85
$Fe^{3+}(2)$–O(10)–P(2)–O(2)–$Fe^{3+}(2)$		AF	2	7.08, 110	6.08
$Fe^{3+}(1)$–O(9)–P(3)–O(3)–$Fe^{3+}(2)$		AF	2	6.83, 116	4.41
$Fe^{3+}(2)$–O(3)–P(3)–O(5)–$Fe^{3+}(1)$		F	2	7.00, 106	4.93
$Fe^{3+}(2)$–O(3)–P(3)–O(5)–$Fe^{3+}(2)$		AF	2	7.10, 106	6.14
$Fe^{3+}(1)$–O(9)–P(3)–O(5)–$Fe^{3+}(2)$		F	2	7.14, 116	4.93
$Fe^{3+}(1)$–O(9)–P(3)–O(5)–$Fe^{3+}(1)$		AF	2	7.04, 116	6.14

Note. AF, antiferromagnetic; F, ferromagnetic; *n*, number of interactions per dimer; pathway, distance (Fe–O–P–O–Fe) in angstroms and angle on oxygen or phosphorus in degrees; O(4), O(2), and O(5) are the oxygen atoms of shared faces.

effect, the ionicity of the Fe–O bonds in phosphates is rather high.

The two different quadrupole splitting values ($\Delta = 0.377$ and 0.643 mm/s) indicate that the environment around one iron is more distorted than the other one. This difference is also measured by the calculated distortion indices, $Dis = \sum_{i=1}^{6}((\text{Fe–O})_i - \overline{\text{Fe–O}})^2/6(\overline{\text{Fe–O}})^2$, of each iron coordination polyhedron which are not the same for Fe(1) and Fe(2): $10^4 Dis_{\text{Fe(1)}} = 12$ and $10^4 Dis_{\text{Fe(2)}} = 42$. Since the Fe(2) octahedral coordination is the more irregular geometry, the doublet $\Delta = 0.643$ mm/s should be assigned to Fe(2).

Ordered state. The calculated and observed spectra at 6 K are shown in Fig. 8b. In the data analysis, two magnetic sextets of equal area, one for each crystallographic site, and with width of peaks fixed to 0.27 mm/s, were fitted to the observed spectrum. The relative areas of the lines in each of the two sextets were constrained to be in the ratio 3:2:1:1:2:3 as is required for an unoriented powder sample.

The hyperfine spectral parameters are reported in Table 5.

The two internal hyperfine fields are similar, $H = 55$ T, typical of high-spin iron(III) nearly at the saturation state, in agreement with the neutron diffraction study.

DISCUSSION

We see in Figs. 9a and 9b that the antiferromagnetic dimers of the $[Fe_2O_9]$ face-sharing octahedra units are linked to each other through several exchange pathways.

It is clear that we have to consider many types of interactions in the $Fe_3P_5SiO_{19}$ compound: intra- and interdimer $[Fe_2O_9]$. These magnetic interactions are given in Table 6 and are described by the relevant parameters.

Intradimer Interactions

1. The cation–cation direct interactions are important since the cations separation is relatively small through the common face (distance Fe–Fe = 3.019 Å). These interactions, occurring between two 3*d* half-filled orbitals, are obviously antiferromagnetic, as the transferred electron must be antiparallel to the net spin at both ions (Goodenough rules (23)).

2. The cation–anion–cation interactions are characterized by the angles Fe–O–Fe near 90° (Table 6); accordingly they are moderately antiferromagnetic, thanks to delocalization superexchange, and partly to correlation superexchange (Goodenough rules (23)).

Interdimer Interactions

There are several Fe–O–P–O–Fe paths connecting each $[Fe_2O_9]$ to its neighbors. As reported in the crystallographic study, the $[Fe_2O_9]$ units form infinite rows, parallel to the *c* axis, connected to each other by PO_4 tetrahedra

(Fig. 9a). The iron atoms in each row are linked to each other through three Fe–O–P–O–Fe pathways, like Fe–O(3)–P–O(9)–Fe (Fig. 9b and Table 6), which are antiferromagnetic. These AF interdimer interactions are probably weaker than the AF direct intradimer interactions and are called super-superexchange type.

The $[Fe_2O_9]$ units in adjacent rows are also linked by PO_4 tetrahedra (Fig. 9a) and the magnetic interactions between them are also assured by super-superexchange Fe–O–P–O–Fe. We see in Fig. 9b that two superexchange pathways which go through each O(5) atom are respectively ferro- and antiferromagnetic. The geometric characteristics of these pathways being almost the same (Table 6), there is, in this case, a frustration phenomenon. There is the same frustrated magnetic super-superexchange phenomenon for all the pathways which go through the oxygen atoms belonging to the common faces of the $[Fe_2O_9]$ units: O(2), O(4), and O(5) (Table 6). It will be interesting to propose a theoretical model to explain these results.

ACKNOWLEDGMENTS

We are grateful to the Institut Laue Langevin (Grenoble) for the provision of neutron facilities.

REFERENCES

1. L. K. Elbouaanani, B. Malaman, and R. Gérardin, *J. Solid State Chem.* **147,** 565 (1999).
2. R. Glaum and A. Schmidt, *Acta Cryst. C* **52,** 762 (1996).
3. A. Leclaire, H. Chahboun, D. Groult, and B. Raveau, *J. Solid State Chem.* **65,** 168 (1986).
4. S. L. Wang, C. C. Wang, and K. H. Lii, *J. Solid State Chem.* **74,** 409 (1988).
5. H. M. Rietveld, *J. Appl. Crystallogr.* **2,** 65 (1969).
6. J. Rodriguez-Carvajal, Fullprof Program, Laboratoire Leon Brillouin, 1998.
7. G. Le Caer, private communication.
8. G. Sheldrick, Shelxs 97 and Shelxl 97, Programs for the Refinement of Crystal structure, Univ. Göttingen, Germany, 1997.
9. R. H. Blessing, *Crystallogr. Rev.* **1,** 3 (1987).
10. J. A. Ibers and W. C. Hamilton, "International Tables for X-Ray Crystallography," Vol. 4. Kynoch, Birmingham, 1976.
11. I. D. Brown and D. Altermatt, *Acta Crystallogr. B* **41,** 244 (1985).
12. L. K. Elbouaanani, B. Malaman, and R. Gérardin, *J. Solid State Chem.*, submitted.
13. M. Ijjaali, B. Malaman, C. Gleitzer, and M. Pichavant, *Eur. J. Solid Inorg. Chem.* **26,** 73 (1989).
14. D. Corbridge, *Bull. Soc. Fr. Miner. Crist.* **94,** 271 (1971).
15. A. Leclaire, J. C. Monier, and B. Raveau, *Acta Crystallogr. B* **40,** 180 (1984).
16. A. Leclaire, M. M. Borel, A. Grandin, and B. Raveau, *Mater. Chem. Phys.* **12,** 537 (1985).
17. A. Leclaire, M. Lamire, and B. Raveau, *Acta Crystallogr. C* **44,** 1181 (1988).
18. M. Cavellec, C. Egger, F. Linares, M. Nogues, F. Varret, and G. Ferey, *J. Solid State Chem.* **134,** 349 (1997).
19. M. Riou-Cavellec, M. Sanselme, J. M. Grenèche, and G. Ferey, *Solid State Sci.* **2,** 717 (2000).
20. L. K. Elbouaanani, B. Malaman, and R. Gérardin, *J. Solid State Chem.* **148,** 455 (1999).
21. F. Menil, *J. Phys. Chem. Solids* **46,** 763 (1985).
22. C. Gleitzer, *Eur. J. Solid Inorg. Chem.* **28,** 77 (1991).
23. J. B. Goodenough, "Magnetism and the Chemical Bond." Interscience Publishers, New York, 1966.